Chapter 8
Mössbauer Spectroscopy

João Carlos Waerenborgh, Pedro Tavares and Alice S. Pereira

8.1 Introduction

Mössbauer spectroscopy is based on nuclear resonance involving the emission and absorption of γ radiation.

The nuclei of the atoms of the same chemical element have the same number of protons, the atomic number. Nuclei of Fe atoms, for example, have 26 protons. However, the number of neutrons in the nuclei of the same element may vary. A nuclear species, or nuclide, is defined by both numbers. It is represented by the chemical symbol of the element, which defines the number of protons, preceded by the total number of nucleons, the atomic mass number. For example, ^{57}Fe refers to the Fe nuclide with mass number 57, i.e., 26 protons + 31 neutrons = 57 nucleons. The most common nuclide of Fe is ^{56}Fe with 26 protons + 30 neutrons. Atoms of ^{56}Fe and ^{57}Fe have the same chemical behavior but the nuclides have quite different properties.

Like the electron cloud in atoms, nuclei are quantum systems and can only have discrete values of energy characteristic of each nuclide. When an atom decays from an excited to the ground electronic state it emits radiation that can be absorbed by an identical atom in the ground state which in turn decays re-emitting radiation with the same energy. This phenomenon of resonance was evidenced by Wood in 1904

J. C. Waerenborgh (✉)
Departamento de Engenharia e Ciências
Nucleares, Centro de Ciências e Tecnologias Nucleares, Instituto Superior Técnico, Universidade de Lisboa, Estrada Nacional 10 (km 139,7), 2695-066 Bobadela LRS, Portugal
e-mail: jcarlos@ctn.tecnico.ulisboa.pt

P. Tavares · A. S. Pereira
Molecular Biophysics Laboratory, UCIBIO/Requimte, Department of Chemistry, Faculdade de Ciências e Tecnologia, Universidade NOVA de Lisboa, 2829-516 Caparica, Portugal
e-mail: pabt@fct.unl.pt

A. S. Pereira
e-mail: masp@fct.unl.pt

A. S. Pereira et al. (eds.), *Radiation in Bioanalysis*, Bioanalysis 8,
https://doi.org/10.1007/978-3-030-28247-9_8

with the yellow spectral emission line of Na. In the same way, a nucleus decays from an excited to the ground state releasing energy, either emitting electromagnetic radiation, γ radiation, which can be absorbed by an identical nucleus, or by ejecting an electron from the corresponding atom, the internal conversion electron.

In contrast to electron resonance, nuclear resonance or γ resonance between identical nuclides was observed experimentally long after it was suggested and even then only under very special conditions. Why did the nuclei refuse to cooperate?

If the energy of the photons emitted by a large number of motionless identical nuclei or atoms in the same excited state is recorded, a curve analogous to that of Fig. 8.1, a Lorentzian curve, described by the Breit-Wigner's expression, is observed

$$W(\varepsilon) = \frac{\Gamma_n^2/4}{(\varepsilon - \varepsilon_o)^2 + \Gamma_n^2/4} \tag{8.1}$$

The most probable energy of the emitted photons is equal to the energy difference between the excited and ground levels, $\varepsilon_o = E_{ex} - E_g$. Γ_n is the width at half-height of the curve, the energy uncertainty, typical of quantum systems. The observation of Γ_n is explained by Heisenberg's uncertainty principle. Since the excited state does not have an infinite lifetime, the energy cannot be determined with as high a precision as we wish. The minimum error with which it is possible to determine ε_o is given by Γ_n, according to

$$\Gamma_n \cdot \tau_\mathrm{n} = h/(2 \cdot \pi) \tag{8.2}$$

where h is the Planck constant and τ_n is the half-life of the excited state.

The probability of γ photons absorption with energy ε_o by nuclei in the ground state identical to those used in the previous experiment, is given by a curve similar to that of Fig. 8.1 and also centered in ε_o.

Radiation emission and absorption curves for motionless systems are therefore similar and overlap in an energy diagram. The behaviour of real systems is, however, more complex.

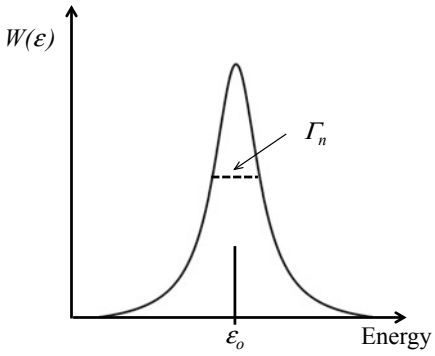

Fig. 8.1 The emission spectrum of an excited nucleus has the shape of a Lorentzian curve. The non-zero halfwidth of this curve, Γ_n, is due to the energy uncertainty of the excited state

A photon of energy ε_o has a linear momentum $p = \varepsilon_o/c$ where c is the speed of light in vacuum. When an atom or nucleus initially at rest emits a photon, in order to conserve the linear momentum of the system, the atom must recoil in the opposite direction to the emission, with a linear momentum p equal to that of the photon. The most suggestive macroscopic image of this phenomenon is the recoil of a firing weapon. If the atom recoils, its kinetic energy varies

$$\varepsilon_R = \frac{p^2}{2M} = \frac{\varepsilon_o^2}{2c^2 M} \tag{8.3}$$

ε_R is the recoil energy and M the mass of the nucleus, practically equal to that of the corresponding atom. Energy conservation now comes into play. What is the source of the energy needed for this recoil? The electronic or nuclear transition. This means that actually the photon will only be emitted with the energy

$$\varepsilon_{em} = \varepsilon_o - \varepsilon_R = \varepsilon_o - \frac{\varepsilon_o^2}{2c^2 M}$$

A similar analysis for the absorbing nucleus leads to the conclusion that the photon, in order to be absorbed, should have the transition energy plus the recoil energy of the absorbing nucleus, i.e., $\varepsilon_{abs} = \varepsilon_o + \varepsilon_R = \varepsilon_o + \frac{\varepsilon_o^2}{2c^2 M}$.

The energies corresponding to the maxima of the emission and absorption curves thus differ by $\frac{\varepsilon_o^2}{c^2 M}$ and this explains why the observation of nuclear resonance is so difficult. While the emission of a visible photon with an energy ε_o of the order of a few eV corresponds to a recoil energy $\varepsilon_R \approx 10^{-10}$ eV, the emission of a γ photon with an energy $\varepsilon_o \approx 10$ keV is related to a recoil energy $\varepsilon_R \approx 10^{-3}$ eV. The half-lives of the excited electronic and nuclear states are of the same order of magnitude (1–100 ns) corresponding, according to Eq. 8.2, to an energy uncertainty $\Gamma_n \approx 10^{-9}$ to 10^{-8} eV. The recoil energy associated with the emission of a γ photon is much higher than Γ_n whereas, in the case of the emission of a visible photon, it is lower than Γ_n. This means that while for optical resonance the emission and absorption curves practically overlap, for nuclear resonance they are far apart (Fig. 8.2). The overlapping integral of $W_{em}(\varepsilon)$ and $W_{abs}(\varepsilon)$, η, which is proportional to the probability of nuclear resonance,

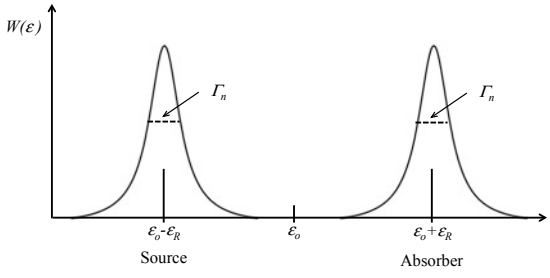

Fig. 8.2 Emission and absorption curves considering the recoil effect when $\varepsilon_R \gg \Gamma_n$

is very low, typically $\eta \sim 10^{-11}$, thus explaining why this phenomenon is very difficult to detect.

Another phenomenon also has a significant impact in resonance experiments. In a real system, due to thermal motion, even before the emission or absorption of a photon the atoms are already moving relative to each other. The well-known Doppler effect increases the frequency of a sound when the emitting source approaches us and decreases its frequency when the source moves away. Likewise, when an emitting nucleus is moving relative to the absorbing nucleus, the photon emitted with a frequency $\cdot\nu_o$ and therefore an energy $\varepsilon_o = h \cdot \nu_o$ will have, from the point of view of the absorber, a higher energy, given by

$$\varepsilon = \varepsilon_o + \frac{\varepsilon_o V_x}{c} \tag{8.4}$$

where V_x is the velocity of the source relative to the absorber. V_x is positive if the nuclei are moving closer and negative if they are moving away. In a gas, as the motions of the atoms are random, V_x shows a nearly continuous range of positive and negative values which may be described by a Maxwell distribution. The resulting distribution of $\frac{\varepsilon_o V_x}{c}$ values (Fig. 8.3) will thus lead to broadening of the emission and absorption curves and consequently to a reduction of their maximum intensity, as the area below the curves remains constant, equal to the total number of nuclei in the system. As the temperature of the system increases, so does the probability of particles reaching higher velocities and, therefore, the thermal broadening of the emission and absorption curves also increases. In optical resonance, where the curves are practically overlapping, the effect of the thermal motion is only a slight reduction of the overlap integral η due to the reduction of the curves intensities close to ε_{em} and ε_{abs}. In the case of nuclear resonance, however, where the maxima of the curves are far apart, their broadening leads first to an increase in the range of energies in which there is a significant overlap of the curves (Fig. 8.3) favoring the increase of η. However, this increase only occurs up to a certain temperature value, T_{opt}, above which the effect of reducing the intensity of the curves around ε_{em} and ε_{abs} becomes predominant.

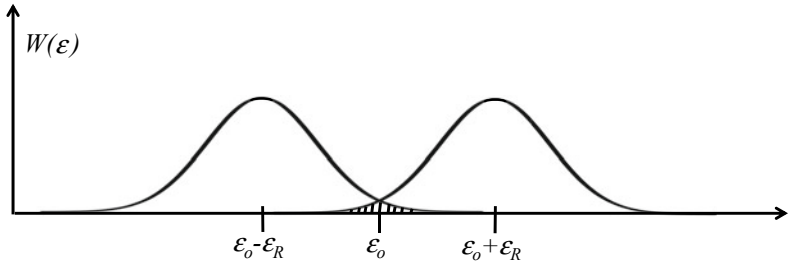

Fig. 8.3 Emission and absorption curves considering recoil and broadening by the thermal Doppler effect

This analysis has not only explained the failure of the first attempts to observe nuclear resonance but also suggested possibilities to get around the difficulties. In fact, nuclear resonance was eventually observed in three kinds of tests: (i) the source was moved towards the absorber with a velocity high enough to compensate the recoil energy by the Doppler effect; (ii) the source and the absorber were heated or cooled to temperatures near T_{opt}; (iii) the occurrence of a preceding nuclear decay or particle reaction conveyed a velocity to the nucleus that compensated the recoil energy by the Doppler effect. These experiments, however, are difficult to perform. In the first case the velocity of the source must be very high, e.g. of the order of 10^5 cm/s for ^{191}Ir; in the last two cases the resonance probability was very low, e.g. for ^{119m}Sn at $T_{opt} = 28$ K this probability is only $\eta \sim 10^{-6}$.

8.2 Mössbauer Effect

In 1957 in Heidelberg, Rudolf Mössbauer was studying for his *PhD* thesis the resonance of the $\varepsilon_o = 129$ keV transition of ^{191}Ir in metallic Ir, for which $T_{opt} = 550$ K. Contrary to expectations, the resonance increased when the temperature dropped from 300 to 78 K. On the other hand if the source was moving relative to the absorber no resonance was observed (Frauenfelder 1962).

How to explain this effect? This discovery, thanks to which Mössbauer was awarded the Nobel Prize for Physics in 1961, was by no means unexpected. Lamb in 1938 had developed the theory of resonance absorption of slow neutrons in crystals, demonstrating that it is possible to observe absorption lines with the natural width. X-ray diffraction technique had also shown that while the intensity of the diffraction lines decreased with increasing temperature their width did not. All the theoretical formalism was available but before Mössbauer no one thought to apply it to γ resonance. At the time, in Nuclear Physics there was a general tendency to ignore the chemical bonds of the atoms whose nuclei were investigated. This was understandable considering that the energies involved in nuclear reactions are several orders of magnitude higher than the energies of chemical bonding. Before the Mössbauer experiment whenever nuclear phenomena were studied, only free atoms were considered.

The cornerstone of the discovery of the Mössbauer effect, the explanation of the unexpected and startling observation with ^{191}Ir, lies on a change of perspective that led to the realization that some nuclear phenomena do not necessarily happen on a different scale from those of atomic phenomena, their energy being comparable to the energies of chemical bonding or the atomic vibrations in solids (Wertheim 1964).

Thus, in the case of emission or absorption of γ photons, the recoil energy transmitted to a free nucleus is usually sufficient to destroy the resonance conditions, unless the atom is incorporated in the lattice of a crystalline or amorphous solid. The energies of the chemical bonds in a solid are of the order of 1–10 eV, considerably higher than the recoil energy $\varepsilon_R \approx 10^{-4}$ to 10^{-1} eV of a free atom that emits a γ photon with energy lower than 200 keV, the case of transitions for which the Möss-

bauer effect is observed. This means that the chemical bonds will not be broken, the emitting nucleus cannot recede freely, and the momentum associated with the emission of the photon will be transmitted to the entire lattice. Instead of the mass M of an isolated nucleus the mass M_C of the whole atom domain must be considered. These domains are typically comprised of more than 10^{15} atoms and therefore their recoil energy will be about 10^{15} times lower than that of an isolated nucleus (Eq. 8.3), i.e., even smaller than the natural line width Γ_n.

Although chemical bonds may not be broken, excitation of phonons occur since ε_R is of the same order of magnitude of the atomic vibration energies, i.e., ε_R may be dissipated by heating the lattice. When there is emission/absorption of γ rays there is a finite probability for zero-phonon events, which is called the recoil-free or recoilless emission/absorption. In these cases resonance is observed. The probability of recoilless events, the recoilless factor f, decreases with increasing ε_R, i.e. with increasing γ photon energy. When ε_R is high enough all the emission/absorption of γ photons takes place with phonon excitation and no resonance is observed. Using the simple Debye model for the thermal vibrations the following dependence of the recoilless factor on temperature, on recoil and on phonon energies, is deduced (Fig. 8.4)

$$f = exp\left[-\frac{\varepsilon_R}{k_B\theta_D}\left(\frac{3}{2}+\frac{\pi^2T^2}{\theta_D^2}\right)\right] \quad T < \theta_D$$
$$f = exp\left(-\frac{6\varepsilon_R T}{k_B\theta_D^2}\right) \quad T > \theta_D \tag{8.5}$$

where θ_D is the Debye temperature of the solid (Greenwood and Gibb 1971). θ_D is higher for solids with stronger chemical bonds and higher phonon energies. The probability of recoilless events increases therefore with θ_D. f decreases with increasing ε_R and with increasing temperature thus explaining the temperature dependence observed by Mössbauer in his experiment with ^{191}Ir.

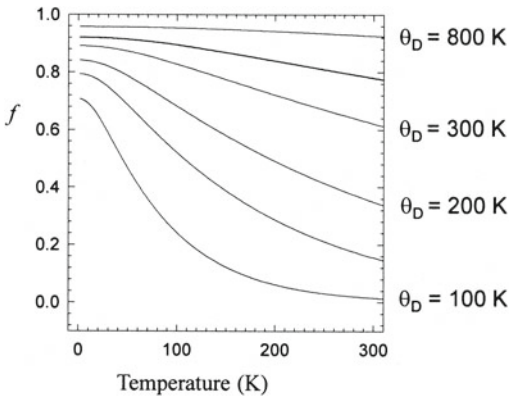

Fig. 8.4 Temperature dependence of the recoilless factor f for different Debye temperatures θ_D

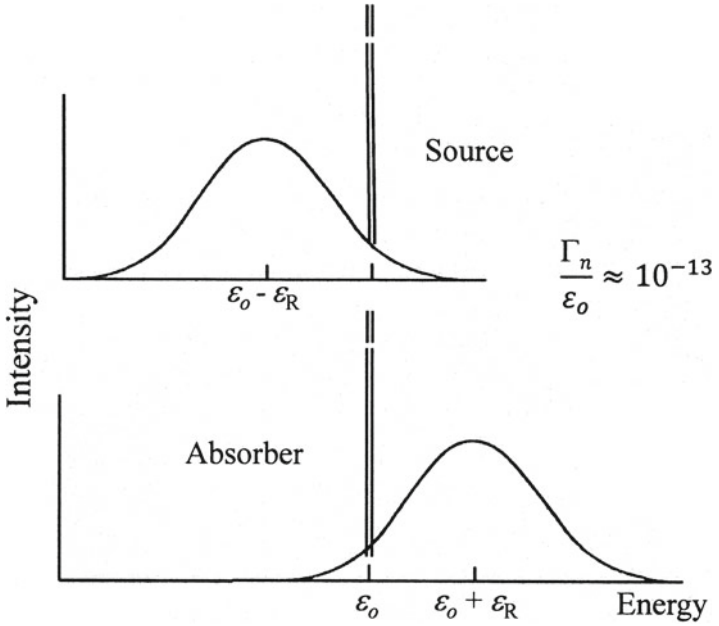

Fig. 8.5 γ ray emission and absorption spectra in a solid lattice. The energy of the recoilless emission and absorption lines is measured with a precision up to $1{:}10^{13}$

When resonance is observed the only energy loss during emission is the recoil of the lattice which is negligible compared to Γ_n. Therefore, the zero-phonon component of the γ emission spectrum has exactly the energy of the nuclear transition with an uncertainty or linewidth determined alone by the widths of the nuclear levels involved in the transition ~2 Γ_n (Fig. 8.5). This line overlaps a band due to thermally excited events with an effective width of the order of the phonon energies. The fraction of the area of the emission spectrum corresponding to the line with $2 \cdot \Gamma_n$ half width is equal to the recoilless fraction f of the source. A similar result is obtained for the absorption spectrum.

8.3 Mössbauer Spectroscopy

The Mössbauer effect consists on the observation of recoilless nuclear resonance with lines with natural linewidth.

The important applications of the Mössbauer effect, which earned R. Mössbauer the Nobel Prize, result from the aforementioned possibility of measuring energies ε_o with a resolution of $\Gamma_n/\varepsilon_o \sim 10^{-11}$ to 10^{-13}. Such a degree of precision allows the observation of relativistic effects in laboratory scale experiments (Greenwood and Gibb 1971). For example, an experiment placing a radiation source and absorber at

different heights, a few tens of meters apart, allows the measurement of the gravitational red shift. The experimental values confirm within 99.7% accuracy those predicted by the theory.

However, the most important application of the Mössbauer effect arises from the possibility of measuring hyperfine interactions, i.e., the electrostatic and magnetic interactions between a nucleus and the electron cloud. These interactions cause small shifts and splittings of the nuclear energy levels which for many nuclides are larger than the natural width Γ_n.

If the emitting and absorbing nuclei are located in atoms with different chemical environments the hyperfine interactions in the source and absorber are different. If this difference is larger than Γ_n the nuclear resonance will not be observed when the source and absorber are stationary. However, differences in hyperfine interactions may be compensated by a Doppler effect resulting from a mechanical motion of the source relative to the absorber with precisely controlled velocity.

The basic configuration of a transmission spectrometer consists of a source containing the studied nuclide in the first excited state. The source is mounted at the end of the movable shaft of a vibrator, the velocity transducer. The absorber is placed as shown in Fig. 8.6, between the source and a γ radiation detector. The source is moved back and forth following a variable periodic velocity while the absorber is kept stationery. If chemically identical, single line, source and absorber are used, the counting rate measured by the detector as a function of the velocity of the source varies according to the curve shown in Fig. 8.6. A maximum absorption is measured when the relative velocity V between source and absorber is zero. As V increases the absorption decreases and when $|V| > (2\,\Gamma_n\,c)/\varepsilon_o$ the Doppler effect (Eq. 8.4) modifies the frequency of the γ radiation by twice the natural line width and resonance condi-

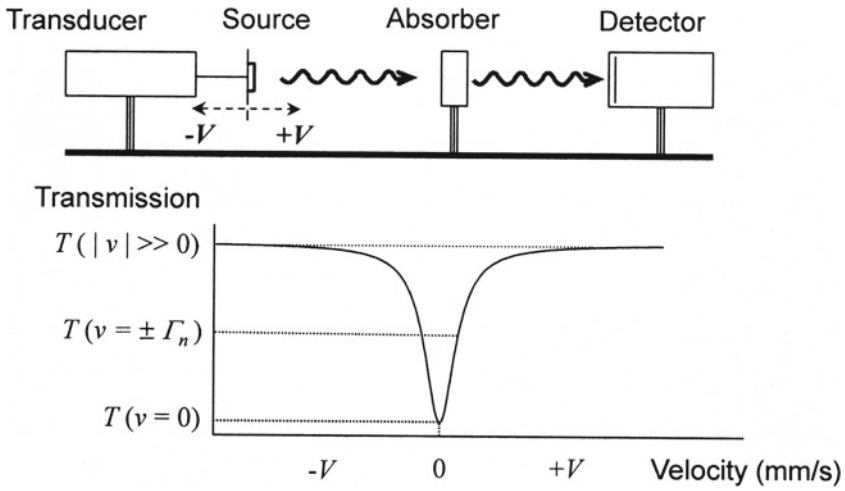

Fig. 8.6 Basic setup of a Mössbauer spectrometer (top) and spectrum (bottom) obtained with a single line source and absorber which are chemically identical

tions are no longer met. In the case of ^{57}Fe, $\varepsilon_o = 14.4$ keV, $\Gamma_n = 9.1 \times 10^{-9}$ eV the Doppler velocity corresponding to Γ_n is 0.095 mm/s. For $V > 0.2$ mm/s resonance is no longer observed. Under ideal conditions the curve is Lorentzian (Fig. 8.1) with twice the width of the emission or absorption curves.

If the absorber is chemically different from the source the maximum absorption, i.e., resonance, will be observed for $V \neq 0$, a velocity value related to a Doppler effect which compensates the difference in hyperfine interactions. In the case of the 14.4 keV transition of ^{57}Fe, velocities within the ± 15 mm/s range are suitable for measuring hyperfine interactions in almost all known Fe-containing materials.

Using a reference material as a single line source the velocity values where resonance is observed give us a wealth of information concerning the oxidation and electronic states of the atoms containing the probed nucleus, the chemical bonds and coordination, and often the atomic magnetic moments and magnetic sublattices of a sample, as shown below. On the other hand, in many instances it is also possible to identify Fe-containing phases based on their typical spectra which may be particularly relevant whenever their identification by other techniques such as X-ray diffraction is not possible.

8.3.1 Isomer Shift

The first hyperfine interaction is the electric monopole interaction. The energies of the nuclei ground and excited states depend on the electron density at the nuclei. Since the ^{57}Fe nucleus is larger in the ground state than in the first excited state, the electrostatic interaction is stronger for the former state as shown in Fig. 8.7.

Let us consider a source where Fe is in the metallic state and an absorber where Fe is in the formal 3+ oxidation state. The electron configurations may be described to a first approximation as [Ar]$4s^2 3d^6$ for metallic Fe and [Ar]$3d^5$ for Fe^{3+}. The s and relativistic $p_{1/2}$ electrons are the only ones with non-zero electron charge density at the nuclei. This means that the nucleus/electron cloud interaction in Fe^{3+} with no $4s$ electrons, is lower than in metallic Fe. Considering the relative sizes of ^{57}Fe nuclei in the ground and first excited states the energy of the nuclear transition in metallic Fe is lower than in Fe^{3+} (Fig. 8.7). Since this energy difference ΔE_δ is higher than Γ_n no resonance would be observed if the source and absorber were standing still. If the source moves towards the absorber with the velocity V, such that the Doppler effect compensates the energy difference

$$\Delta E_\delta = \frac{\varepsilon_o \cdot V}{c}$$

resonance is established and an absorption peak is observed. This velocity V is called the isomer shift, *IS*, of Fe^{3+} in the absorber relative to the source we are using. If in the absorber there was Fe^{2+}, electronic configuration [Ar]$3d^6$, the number of s electrons would be the same as in Fe^{3+}. There is however one additional d electron in Fe^{2+}. d

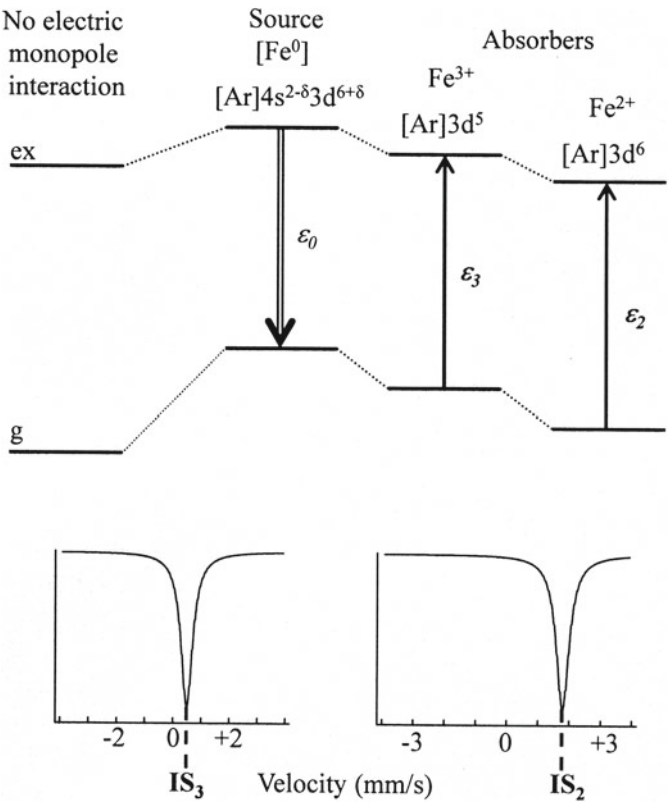

Fig. 8.7 Nuclear levels considering no electric monopole interaction and considering this interaction for different electronic states of the Fe atoms (top). Isomer shift values IS_3 and IS_2 for high-spin Fe^{3+} and Fe^{2+}, respectively (bottom, see text)

electrons have zero probability at the nucleus but they have a shielding effect on the *s* electrons. A fraction of *s* electron density, particularly 3*s* electron density is further away from the nucleus than 3*d* electrons. The electrostatic repulsion that *s* electrons experience there depends on the screening effect of inner electrons. When the *d* electron density increases the shielding effect also increases causing an expansion of the *s* electrons and a decrease of the *s* electron density at the nucleus. As shown in Fig. 8.7 this implies that the energy of the nuclear transition is higher in Fe^{2+} than in Fe^{3+}. The *IS* of Fe^{2+} is therefore higher than the *IS* of Fe^{3+}.

The IS value also depends on the electronegativity of the ligands and the coordination of the Fe atoms. Normally for both oxidation states IS decreases with decreasing coordination number and decreasing electronegativity of the ligands, which can be understood as resulting from a higher degree of covalence of the bonds. Nevertheless the ranges of *IS* values for the Fe^{2+} and Fe^{3+} in the so-called high-spin state, where the electron configurations for Fe^{2+} and Fe^{3+} are closer to the formal [Ar]3d^6 and [Ar]3d^5, are clearly distinct (Gütlich et al. 2011). These high-spin states are observed

in compounds with predominant ionic bonds such as Fe oxides, hydroxides, silicates, phosphates, sulphates, etc. where the ligand field is weak, weaker than the spin coupling energy. In these compounds Fe^{2+} and Fe^{3+} are thus readily distinguished on the basis of their *IS* values.

In compounds where the chemical bond has a significant covalent character Fe^{2+} and Fe^{3+} are in the so-called low-spin state, the electron sharing between the Fe cations and the ligands becomes significant, the 4*s* electron orbitals occupancy is no longer zero which causes a significant decrease of *IS*. In addition to the *s* orbital population the relative importance of *p* and *d* orbitals in the bonding as well as the extent to which the electrons are delocalized play a role in determining the *IS* value. As a result, the range of *IS* values for low-spin Fe^{2+} and Fe^{3+} are very similar and overlap the lower *IS* values of high-spin Fe^{3+} (Gütlich et al. 2011).

IS values are generally given as velocities, units mm/s, according to Baggio-Saitovitch et al. (2002) and are commonly given relative to the metallic αFe standard, the same standard used for velocity calibration as referred below.

8.3.2 Quadrupole Splitting

The second hyperfine interaction is the electric quadrupole interaction. As for electrons in an atom where the quantum number *J* specifies the total angular momentum (orbital + spin), for nuclei the quantum number *I* defines the nuclear spin. The distribution of nuclear charges may have a non-spherical symmetry. This is the case for the ^{57}Fe nucleus in the 14.4 keV state, with $I = 3/2$, whose nuclear charge distribution is observed as a prolate ellipsoid (Fig. 8.8) thus presenting a positive electric quadrupole moment *Q*. If the electric charge distribution around the nucleus has neither spherical nor cubic symmetry, i.e., if it gives rise to an electric field gradient $\nabla.\boldsymbol{E}$ at the nucleus position, the nucleus/electron cloud interaction energy depends on the direction of the nucleus spin relative to the electronic and lattice charge distributions.

Let us assume an electric charge distribution with axial symmetry in which there is a larger concentration of negative charge along the axis of symmetry, the *z* axis (Fig. 8.8). In a classical system any orientation of the nucleus relative to that axis would be possible. Since we are dealing with a quantum system, the nucleus can only adopt a discrete number of orientations, determined by the value of the spin quantum number which for the 14.4 keV state is $I = 3/2$. Each of those orientations is, in turn, defined by the m_I values (−3/2, −1/2, 1/2 and 3/2). Note that for $m_I = 3/2$ the nuclear charge distribution is on the average closer to the *z* axis of the system than when $m_I = 1/2$. Since the density of negative charges along this axis is the highest, the configuration $m_I = 3/2$ corresponds to a lower energy of the system (energy diagram in Fig. 8.8), as it increases the attractive interaction between the negative electronic charges and the positive nuclear charge. $m_I = -1/2$ corresponds to an inversion in the direction of the magnetic moment of the nucleus relative to $m_I = 1/2$, which, from the point of view of the average distribution of the nuclear charges has no effect on the interaction energy with the electric field gradient. The

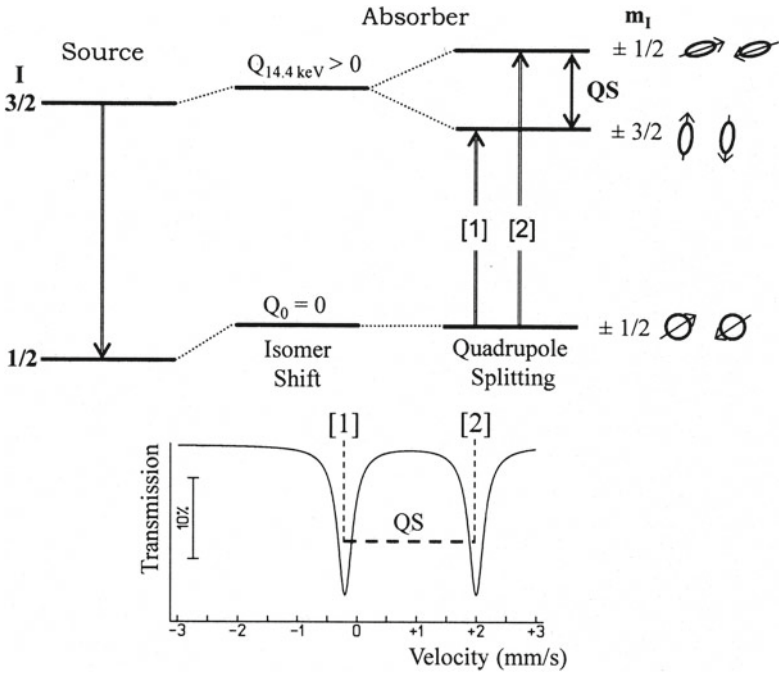

Fig. 8.8 Electric quadrupole interaction in the case of an $\nabla.\boldsymbol{E}$ with higher negative charge density along the z axis than on the perpendicular plane (top, see text). Quadrupole doublet observed in the Mössbauer spectrum (bottom) for this $\nabla.\boldsymbol{E}$ in the case of randomly oriented powder samples with no anisotropic f factors

energy of the system is therefore equal for both $m_I = \pm 1/2$ substates. The same is true for $m_I = \pm 3/2$.

Therefore, when the position occupied by Fe in the solid lattice has point symmetry lower than cubic, the degeneracy of the first excited state of the ^{57}Fe nucleus is partially raised and two sublevels with different energies are observed (Fig. 8.8). Since in the ground state the nucleus has spin $I = 1/2$, no interaction with an $\nabla.\boldsymbol{E}$ is observed. This is easy to understand since m_I may only have two symmetric values $\pm 1/2$. The nucleus behaves as if its quadrupole moment is zero and the nuclear charge distribution is spherical.

This means that in the Mössbauer spectra of a sample where Fe is in a position with symmetry lower than cubic two lines, one doublet, is observed (as long as no magnetic interactions are observed, see below). The energy difference between both lines of a doublet is called the quadrupole splitting, QS, measured in mm/s as the isomer shift. When the coordination polyhedron of the Fe cation is a distorted octahedron or tetrahedron, or even when it is a regular polyhedron but the ligands of Fe are not all the same, a non-zero QS is observed. For example, in the spectra of $[Fe(CN)_6]^{4-}$ or $[Fe(CN)_6]^{3-}$, where the octahedral configuration of the 6 CN^- ligands has cubic symmetry, only one line is observed. The substitution of one of the CN^- ligands by

NO^+ in $[Fe(CN)_5(NO)]^{2-}$ creates a charge distribution asymmetry even if the six ligands are at the corners of a regular octahedron, and in the corresponding spectrum a doublet is observed.

The value of *QS* depends on the degree of asymmetry and the electronic state of Fe. Each of the five 3*d* orbitals of high-spin Fe^{3+} has one electron. The half-filled 3*d* subshell, such as fully filled electronic subshells, creates a spherically symmetric charge distribution, whatever the $\nabla.\boldsymbol{E}$ due to the ligand field or any other lattice electric charge distribution. In this case if *QS* is different from zero there is only the component due to the lattice $\nabla.\boldsymbol{E}_{\boldsymbol{latt}}$ as $\nabla.\boldsymbol{E}_{\boldsymbol{elect}}$ due to the electron cloud is always zero.

In the case of high spin Fe^{2+} there is a sixth electron 3*d*. If the lattice field has spherical symmetry the six 3*d* orbitals have the same energy, their occupancy by the sixth 3*d* electron is the same and no quadrupole splitting is observed. If the symmetry is cubic as in a regular octahedral field the three t_{2g} orbitals (d_{xy}, d_{xz}, d_{yz}) will have lower energy than the remaining 3*d* orbitals, the e_g (d_{x2-y2}, d_{z2}). The occupancy of the three t_{2g} orbitals by the sixth *d* electron is the same and since this set of 3*d* orbitals has cubic symmetry no $\nabla.\boldsymbol{E}$ is observed either. A similar analysis of a cubic tetrahedral field, where the e_g orbitals have lower energy leads to the same conclusion. It is not surprising that if the Fe cation is on a lattice position with cubic symmetry there is neither a lattice $\nabla.\boldsymbol{E}_{\boldsymbol{latt}}$ nor an electronic $\nabla.\boldsymbol{E}_{\boldsymbol{elect}}$. A quadrupole splitting will only be observed if the crystal field is lower than cubic, for instance if there is a tetragonal or trigonal distortion of an octahedral crystal field. If the field is a distorted octahedron the degeneracy of the three t_{2g} orbitals is lifted. Since each one or any set of two t_{2g} orbitals has symmetry lower than cubic the electronic charge distribution also creates a $\nabla.\boldsymbol{E}_{\boldsymbol{elect}}$. *d* electrons are, on average, much closer to the nucleus than the lattice charges around the respective atom. The $\nabla.\boldsymbol{E}_{\boldsymbol{elect}}$ created by the *d* electron is therefore much higher than the lattice one. Hence, under similar conditions for high-spin Fe cations, *QS* of Fe^{2+} is significantly higher than Fe^{3+}. Moreover, when spectra are carried out at different temperatures within a range where the energy difference between the e_g or between the t_{2g} orbitals due to the non-cubic ligand field is of the order of magnitude of the thermal energy $k_b \cdot T$, the *QS* of Fe^{2+} decreases with increasing temperature whereas *QS* of Fe^{3+} remains practically constant. The temperature dependence of the Fe^{2+} *QS* is a result of the temperature dependence of the thermal population of the low-lying first excited electronic state. On the other hand, as long as there is no phase transition *QS* of high-spin Fe^{3+} will only slightly change due to the thermal expansion of the lattice.

In compounds where the chemical bond has a significant covalent character a different behaviour is observed. In the case of Fe^{2+} in strong octahedral crystal fields the six 3*d* electrons may fully occupy the lowest energy t_{2g} orbitals. The electronic contribution for $\nabla.\boldsymbol{E}$ is then zero even on a lattice site with non-cubic symmetry. On the other hand, in the case of Fe^{3+} the five 3*d* electrons will not fully occupy the t_{2g} orbitals and an electronic contribution for $\nabla.\boldsymbol{E}$ is expected. Therefore, in the low-spin case, in a distorted octahedral environment *QS* of Fe^{2+} is normally lower than the temperature dependent *QS* of Fe^{3+}.

On the basis of the *IS* and *QS* values high-spin Fe^{2+} may be unambiguously identified. For the remaining electronic states however, namely low-spin Fe^{2+} and Fe^{3+} and high-spin Fe^{3+} the measurement of magnetic hyperfine interactions is necessary.

8.3.3 Magnetic Hyperfine Splitting

This hyperfine interaction is the magnetic dipole interaction. When there is a magnetic field at the nucleus, the hyperfine magnetic field $\boldsymbol{B_{hf}}$, a nuclear Zeeman effect is observed. $\boldsymbol{B_{hf}}$ interacts with the magnetic dipole moment of the nucleus by fully raising the degeneracy of nuclear levels. Each m_I will correspond to a different energy, depending on the angle between the nuclear magnetic moment $\boldsymbol{\mu_{nuc}}$ and $\boldsymbol{B_{hf}}$, as shown in Fig. 8.9. For the ground state of ^{57}Fe $I = 1/2$ ($m_I = -1/2$ and 1/2) there are two sub-levels and for the excited state $I = 3/2$ four ($m_I = -3/2, -1/2$, 1/2 and 3/2). Only six transitions are allowed between the ground and excited sublevels by the selection rules; those corresponding to $\Delta m_I > 1$ are not allowed since the total angular momentum of the γ photon is only 1. These six transitions are observed in a Mössbauer spectrum as a six-line pattern, the sextet, or the magnetic splitting. The relative intensities of these six lines are determined by the transition probabilities between the different sub-levels of the excited and ground states. In a sample consisting of randomly oriented powder the relative intensities are 3:2:1:1:2:3 (Fig. 8.9). The splitting of the six lines is proportional to the value of the modulus of $\boldsymbol{B_{hf}}$.

$\boldsymbol{B_{hf}}$ results from the magnetic moment of the atom. Atoms with full electronic subshells, where all the electron spins are coupled, have zero magnetic moment. This is the case of low-spin Fe^{2+} with electron spin quantum number $S = 0$. A non-zero magnetic moment arises from unpaired electrons on the outer layers which are not fully filled. In addition to their contribution to $\boldsymbol{B_{hf}}$ these electrons polarize the inner shells. The polarization of *s* electrons whose density at the nuclei is non-zero gives rise to the so-called Fermi contact term, the most important contribution to $\boldsymbol{B_{hf}}$.

Except for low-spin Fe^{2+}, the outer electron shells of Fe atoms or Fe^{2+} and Fe^{3+} cations contain unpaired electron spins. This implies that they have a non-zero magnetic moment $\boldsymbol{\mu_{Fe}}$. However, in compounds in the paramagnetic state, which do not exhibit a spontaneous global magnetization, $\boldsymbol{\mu_{Fe}}$ of each atom has, in the absence of an external magnetic field, a random orientation which, with a few exceptions, varies too rapidly from the Mössbauer effect point of view. This means that the frequency of the $\boldsymbol{\mu_{Fe}}$ and resulting $\boldsymbol{B_{hf}}$ changing directions, is higher than 10^8 Hz, the order of magnitude of the nuclear moment precession frequency around $\boldsymbol{B_{hf}}$. In other words the nuclear magnetic moment $\boldsymbol{\mu_{nuc}}$, during its precession movement does not have time to complete a single rotation around $\boldsymbol{B_{hf}}$ before this hyperfine field changes direction several times. In classical physics we might say that the average of the $\boldsymbol{B_{hf}}$ is zero during the time that the nucleus is 'observing' it. Thus, in the Mössbauer spectrum rather than a sextet, one singlet, or if the quadrupole electric interaction is non-zero, a doublet, is observed.

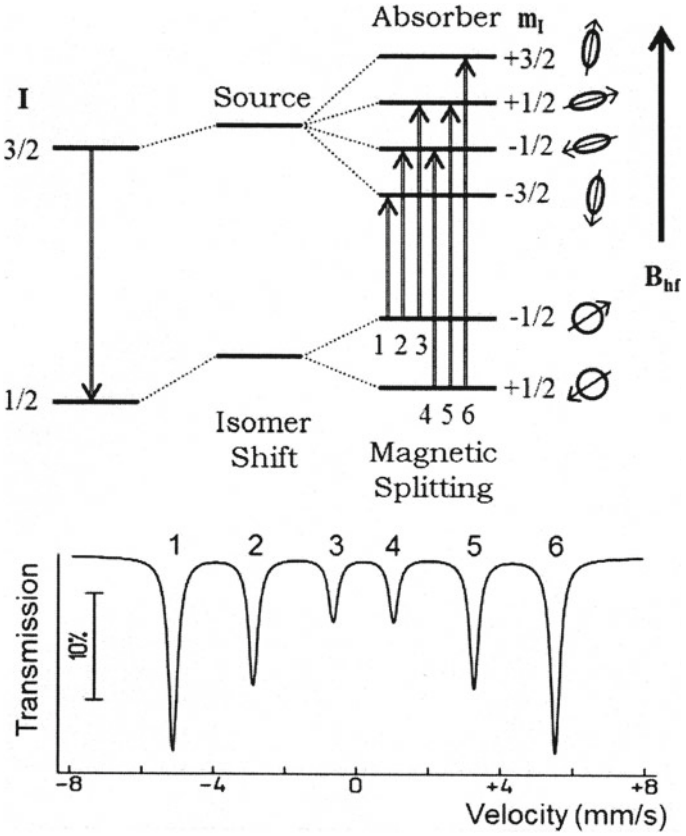

Fig. 8.9 Magnetic hyperfine interaction (top, see text). Magnetic splitting observed in the Mössbauer spectrum (bottom) in the case of randomly oriented powder samples with no anisotropic f factors

When strong, long-range magnetic correlations are established among the Fe atoms the $\boldsymbol{\mu}_{Fe}$ are "frozen" from the Mössbauer effect point of view. The frequency with which their directions change, determined by the magnons frequency, is much lower than 10^8 Hz. This is the case for magnetically ordered materials and for spin glasses. The best known example of a magnetically ordered material at room temperature is magnetite, which attracts iron or non-austenitic steel objects. Many materials only become magnetically ordered at low temperatures.

In a paramagnetic compound an external magnetic field may also slow down the $\boldsymbol{\mu}_{Fe}$ long enough to allow the observation of a magnetic splitting.

While in the case of rare-earths $|\boldsymbol{B}_{hf}|$ is directly proportional to the atom magnetic moment, in the case of Fe the hyperfine magnetic coupling, the constant of proportionality relating $|\boldsymbol{B}_{hf}|$ with $|\boldsymbol{\mu}_{Fe}|$, depends on the electron densities at the bonding orbitals, particularly the 4*s* ones, and therefore on the chemical composition of the material. This dependence however is not high enough to prevent the estimation of

the number of unpaired electrons and therefore the oxidation degree of the Fe cations. Furthermore, within the same compound or in compounds with similar composition and structure, $|\boldsymbol{B_{hf}}|$ increases with increasing $|\boldsymbol{\mu_{Fe}}|$.

αFe is a standard sample whose B_{hf} is known, 33.0 T at room temperature. Calibration of Mössbauer spectra is performed on the basis of the well known velocities of the six lines of the sextet observed for this standard at room temperature.

Usually both electric quadrupole and magnetic dipole interactions are observed. When the $\nabla.\boldsymbol{E}$ is axially symmetric and the quadrupole interaction is significantly lower than the magnetic one it may be treated as a perturbation of the magnetic hyperfine interaction. In this case a sextet is still observed in the spectrum but the centre of gravity of the four inner lines is shifted relative to the centre of gravity of both outer lines. When the quadrupole and magnetic interactions are similar, or when $\nabla.\boldsymbol{E}$ is not axially symmetric and the magnetic axis does not lie along one of the main $\nabla.\boldsymbol{E}$ axes, the position and relative intensities of the absorption lines have to be calculated by solving the complete Hamiltonian for the hyperfine interactions in both the excited and ground nuclear states of the ^{57}Fe nuclei.

8.4 Mössbauer Spectrometer

The basic components of a Mössbauer spectrometer are the source, the γ ray detection system (detector, high voltage source, amplifiers, single channel analyser) the Mössbauer system itself (velocity transducer, drive unit, function generator) and the acquisition system where the spectra are recorded.

The source is a radioactive nuclide which has a long enough half-life and which decays to an excited state of the studied nuclide. At least a fraction of the decays to the ground state of this nuclide takes place through an excited state that allows the observation of the Mössbauer effect. In the case of iron the ^{57}Fe nuclide has two Mössbauer transitions, 136 and 14.4 keV. The former one has no practical application since its energy is high and consequently the recoilless factor very low. Mössbauer spectroscopy is therefore exclusively performed with the 14.4 keV transition. The radioactive nuclide in the source is ^{57}Co with a half-life of 271 days. This source is commercially available. ^{57}Co is produced in a nuclear facility and deposited on a metallic matrix foil chemically inert and with high electric and thermal conductivity in order to minimize the aftereffects of the nuclear decay preceding the Mössbauer γ ray emission. Furthermore, the matrix and the concentration of ^{57}Co should be such that no strong magnetic correlations are established and the source emits a single narrow line. The most common matrixes are Pd or Rh. ^{57}Co (Rh) sources have better recoilless factors and only slightly worse line widths than the Pd ones. Usually sources with an activity of 925 or 1.85 MBq are used. In addition to the 14.4 keV these sources also emit 122 and 136 keV γ-rays as well as Fe and Pd or Rh X-rays. Operation with these sources requires therefore special care. Particularly while mounted in the spectrometer lead shields with appropriate thickness should be used to reduce external radiation exposure to values comparable to the natural

background. While assembling or removing the source from the velocity transducer every reasonable effort to maintain exposures to the ionizing radiation as far below the dose limits as practical should be made.

The most appropriate radiation detector for ^{57}Fe Mössbauer spectroscopy is a proportional counter with krypton or xenon fill gas and a small amount of a so-called quench gas, usually methane. Argon is also suitable as fill gas but requires larger detectors due to its lower absorption cross section for the 14.4 keV radiation. A high voltage supply, a stable low-capacitance preamplifier and amplifier are needed. The height of the voltage pulses output by the detector, amplified by the amplifier units, is proportional to the energy dissipated in the proportional counter by the radiation. The voltage pulses from the amplifier may be collected directly or through a single channel analyzer by an acquisition board associated with a computer where the spectra are displayed. Either this acquisition board or the single channel analyzer selects the voltage pulses within a voltage range corresponding to the photoelectric absorption of the 14.4 keV γ-rays of ^{57}Fe. Only these pulses are accumulated in the acquisition board within a memory composed of different channels (usually 512 or 1024). In the so-called fast multiscaling mode the acquisition boards accumulate these pulses in only one channel at a time. Each channel corresponds to a specific velocity as explained below.

The Mössbauer system itself comprises a velocity transducer, an electromechanical device that imparts the Doppler velocity to the source. When operated in constant acceleration mode this transducer is driven by a symmetric triangular waveform, in such a way that the source is periodically moved in opposite directions, with a velocity that varies linearly with time between a maximum positive and a minimum negative value (Fig. 8.10) relative to a stationary absorber, usually the studied sample, as described above (Fig. 8.6). Positive velocities correspond to movement of the source toward the absorber and negative velocities away from the absorber. A

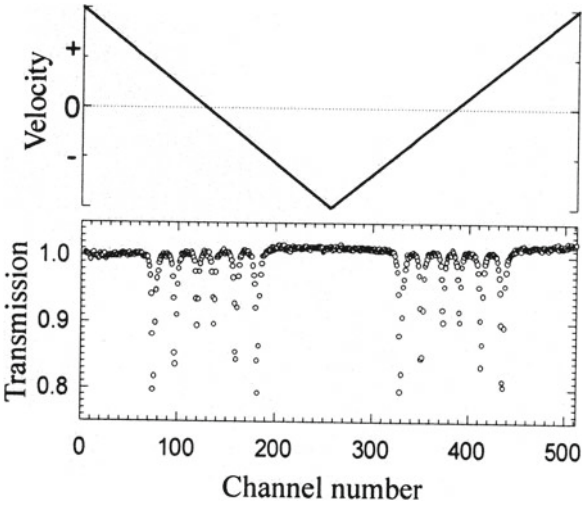

Fig. 8.10 Constant acceleration mode where velocity of the transducer varies linearly with time following a triangular wave form (top). Mirror image spectra are obtained (bottom)

drive unit and a function generator sometimes coupled in the same module control the transducer. Feedback circuitry in these units gets the transducer to follow the waveform precisely. Simultaneously the function generator sends the digital pulses that synchronize the sweeping of the acquisition board memory channels with the source movement, in such a way that each channel always corresponds to the same narrow velocity range. For example, a spectrum collected in a 512 channels memory for velocities between +12 and −12 mm/s. The velocity changes between +12 and −12 mm/s, i.e., 24 mm/s, within each memory half, 256 channels. The velocity gradient per channel is therefore $\frac{24}{256}$ mm/s. Assuming that the detector pulse counts corresponding to linearly decreasing velocity from +12 mm/s down to −12 mm/s accumulate in the first memory half (as shown in Fig. 8.10),

channel 1 corresponds to velocity range between 12 and $12 - \frac{24}{256}$ mm/s
channel 2 corresponds to velocity range between $12 - \frac{24}{256}$ and $12 - 2 \times \frac{24}{256}$ mm/s
… …
channel 256 corresponds to velocity range between $12-255 \times \frac{24}{256}$ and $12-256 \times \frac{24}{256} = -12$ mm/s.

On the 2nd half of the memory a mirror image spectrum is obtained corresponding to linearly increasing velocity from −12 mm/s down to +12 mm/s, when a full period of the to and fro movement is achieved (Fig. 8.10). After reaching +12 mm/s a new memory sweep is restarted from channel 1 and the velocity increases again.

In order to obtain spectra with the absorber at low temperature cryostats are used. For temperatures in the range 1.5–300 K liquid helium bath cryostats are very reliable. The sample is kept in liquid He at 4 K and below or in He exchange gas above 4 K. For measurements above 77 K only liquid nitrogen may be used and the sample is kept in nitrogen exchange gas. Bath cryostats have liquid helium and liquid nitrogen reservoirs within a vacuum chamber. Thermal shields at liquid nitrogen temperature minimize heat transfer by radiation to the helium reservoir. A tube with narrow cross section leads liquid helium from the reservoir to a thermally isolated sample chamber. The liquid He flow is controlled by a needle valve. In order to stabilize a temperature value above 4 K a temperature controller connected to a temperature sensor and a heating coil located in the sample chamber is used. Between 1.5 and 4 K the desired temperature is achieved by keeping a constant value of the He pressure below 1 atm in the sample chamber. Closed cycle or cryogen-free cryo-cooler systems are increasingly popular since their operation is cheaper as no liquid helium is needed and a considerable progress in isolating the sample chamber from the cooler unit vibrations has been achieved.

8.5 Absorber Preparation

Long et al. (1983) have demonstrated that the ideal sample absorber thickness, t_{ideal}, that allows us to obtain the desired results in the shortest time and with the best signal to noise ratio, lies between the reverse of the mass absorption coefficient of

the sample and twice this value. The value of t_{ideal} for samples with high electronic absorption when compared with the resonant Mössbauer absorption should be close to the former value.

In addition to t_{ideal} one should also be careful to avoid saturation effects i.e., spectral distortions due to the thickness effect, such as peak broadening, and to prevent overestimating the absorption areas of the Fe species with lower concentrations in the specimen. Due to its simplicity a rule of thumb considering t_{thick} ~ 1–5 mg/cm^2 of total Fe has been widely used, t_{thick} increasing with the number of spectral lines (Gütlich et al. 2011). In fact, it is still often used when peaks with ideal linewidths and very accurate measurements of the fraction of different Fe species based on the estimated relative areas of the corresponding peaks are not required. When very accurate quantitative results are at stake, in addition to careful calculation of the sample thickness, different recoilless factors for the distinct Fe species and fitting of the spectra with the full transmission integral should be considered (Rancourt et al. 1993).

Very often for biological or medical applications the amount of Fe in the samples is too low to obtain reasonable spectra. In these cases one should bear in mind that natural Fe has four stable isotopes, ^{54}Fe, ^{56}Fe, ^{57}Fe and ^{58}Fe and that their isotopic abundances are, respectively, 5.8%, 91.4%, 2.2% and 0.3%. This means that in natural samples or in compounds synthesized with natural Fe only 2.2% of the total Fe is Mössbauer "active". If the specimens are prepared using Fe enriched in the ^{57}Fe isotope instead of natural Fe t_{ideal} or t_{thick} may be lowered down to ~50 times.

8.6 Mössbauer Spectroscopy of Other Elements

In order to perform Mössbauer spectroscopy the chemical element should have at least one isotope where the Mössbauer effect is observed. The probability of recoilless emission and absorption is only non-negligible for low energy nuclear transitions, typically lower than 200 keV. This is the reason why it is not observed for light nuclides which have no low energy first excited states.

In practice for transitions above 50–60 keV the source or the absorber should be kept at low temperatures, typically liquid helium temperature, as the recoilless factor f increases with decreasing temperature.

The higher the energy of chemical bonds, the higher θ_D, i.e., the higher the energy required to excite thermal vibrations, and therefore the higher f (Eq. 8.5). In the case of ^{57}Fe, for instance, oxide or silicate spectra are easily obtained at room temperature, whereas for many organometallic or protein materials samples are measured at low temperatures in order to obtain in a reasonable time statistically good spectra.

Even when an element has an isotope where the Mössbauer effect is observed it may not be suitable for Mössbauer spectroscopy. This is the case for long-lived excited states with half lives $\tau_N > 10^{-6}$ s where line widths $\Gamma_n < 0.019$ mm/s are so narrow, that a very high precision of the velocity measurement is required or ultimately Γ_n is lower than the recoil energy of the entire lattice and the absorption

and emission lines do not overlap sufficiently. On the other hand, for short-lived excited states $\tau_N < 10^{-11}$ s hyperfine interactions are not observed because their energy is lower than the line widths.

Another issue is the availability of suitable sources for Mössbauer spectroscopy. The source must consist of radioactive nuclei that decay to an excited state of the probed nucleus. This nucleus further decays to the ground state through a cascade of transitions including the Mössbauer transition. In order to allow the collection of spectra the half-life of the parent radioactive nuclide should be long enough. That is the main reason why the only commercially available Mössbauer sources are ^{57}Co, ^{119m}Sn and ^{151}Sm whose half-lives are 271 days, 250 days and 87 years, respectively. For other parent nuclides whose half-lives are shorter or similar to the time necessary to obtain a spectrum a neutron source or a particle accelerator must be available at the same facility as the spectrometer.

Radioactive sources are not necessary if synchrotron radiation is used for Mössbauer spectroscopy. Experiments with synchrotron radiation are discussed in Gütlich et al. (2011).

Finally, the Mössbauer effect can only be observed in solids, crystalline or amorphous, rarely in liquids of high viscosity. The study of samples in solution can only be performed with the sample at a temperature lower than the melting point.

8.7 Mössbauer Spectroscopy of Biological Systems

Mössbauer spectroscopy has been successfully applied to the study of iron containing biological systems, proving to be a powerful tool to investigate the electronic structure of such compounds. As described above, information about magnetism, electronic relaxation, chemical bonding and redox properties can easily be obtained. Historically, Mössbauer spectroscopy was first used to provide a detailed description of oxidation and spin state of heme-containing proteins, which were available in proper quantities to be studied (Lang and Marshall 1966). Iron cofactors oxidation and spin state and character of bonds, electronegativity of ligands and molecular symmetry can be probed by *IS* and *QS*, as seen above. Magnetic hyperfine splitting can add additional information about coupled systems, nuclearity and can be related to results obtained by other spectroscopic techniques.

One of the initial challenges to use Mössbauer spectroscopy to characterize iron-containing proteins was the fact that the natural abundance of the ^{57}Fe isotope is only 2.2% and that Mössbauer spectra need samples with ca. 1 mM iron concentration. A simple calculation points to the fact that a natural abundance sample of a simple mononuclear iron protein needs to be close to 45 mM. In the case of proteins purified from microorganism, and to circumvent this problem, growth media can be supplemented with an ^{57}Fe solution which will enrich the iron cofactors in this isotope. This can be a costly process when applied to large scale growths. Fortunately, overexpression methods are routine laboratory tools to obtain more protein of interest in lab scale batch growths. Thus, over the past decades Mössbauer spectroscopy has

been used to discover new iron cofactors, determining the nuclearity and electronic properties of multi-iron containing centers, unveiling the organization of iron atoms in case of proteins containing multiple iron centers, showing number of attainable redox states and their correspondent redox potential, identifying substrate/inhibitor binding sites, and discovering and characterizing new kinetic intermediate species.

In the next subsections we will cover the known types of iron species studied by Mössbauer spectroscopy, using *IS* and *QS* as a roadmap to the spin and redox state of iron ions and centers (see also Fig. 8.11). It is relevant to note that, for each system, important information can be derived from the magnetic hyperfine splitting interaction and parallel EPR sample data.

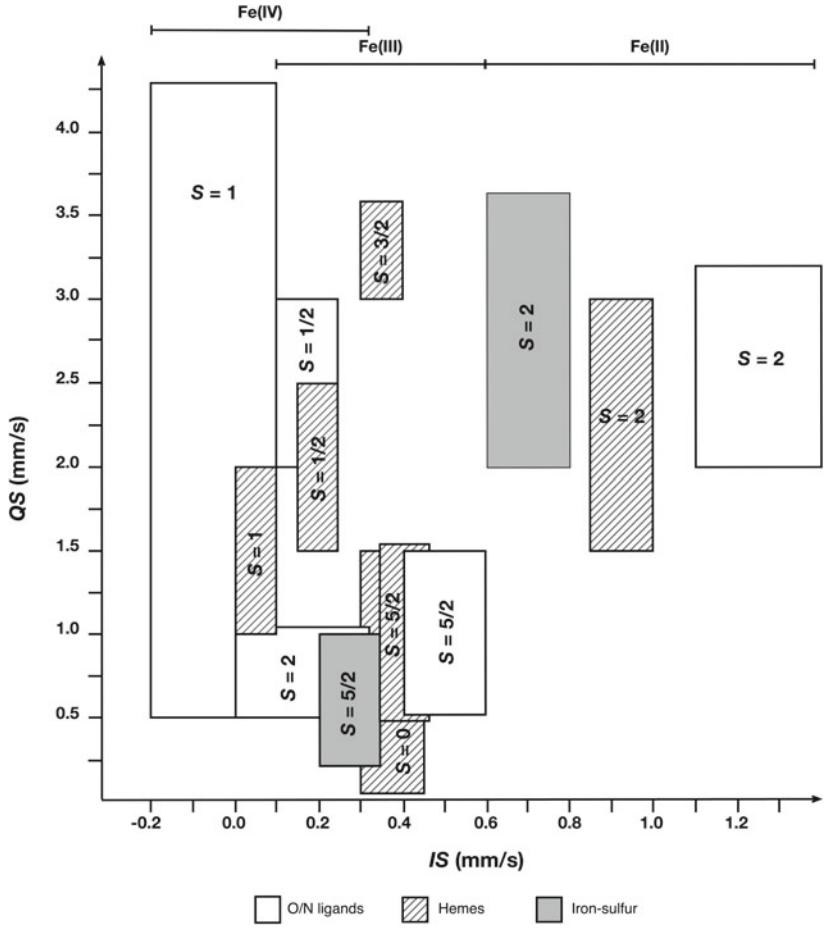

Fig. 8.11 Typical values of *IS* and *QS* for iron centers/types present in biological molecules (heme iron, iron-sulfur centers, iron with N/O ligands). Parameters of valence-delocalized iron-sulfur iron pairs are not included. Additional details can be found in Sect. 8.7. Values are given relative to the centroid of the room-temperature spectrum of a metallic iron foil

Appropriate references are included to direct the reader for further information about each system. Please note that, unless otherwise specified, Mössbauer parameters quoted in the next sections are obtained from data acquired at 4.2 K.

8.7.1 Iron-Sulfur Centers

Iron-sulfur centers (or iron-sulfur clusters) are widespread in nature, being part of several proteins and enzymes (Pandelia et al. 2015). Their role in biology can go from simple electron transfer cofactors to participate in important metabolic pathways such as the citric acid cycle or nitrogen fixation. In many cases the identification of the iron-sulfur center was associated to Mössbauer studies that were capable of distinguish nuclearity and redox states not accessible by other techniques. Simple iron-sulfur centers are characterized by the number of iron and sulfur atoms present in their structure.

The simplest iron-sulfur center, the rubredoxin-type site $FeCys_4$, is constituted by a single iron coordinated by four cysteinyl residues in a tetrahedral coordination. This center can be either in a ferrous or ferric state. In the high-spin ferric state ($S = 5/2$) it has an *IS* ranging from 0.25 to 0.32 mm/s and a *QS* between 0.5 and 0.75 mm/s. Upon one electron reduction, this center becomes high-spin ferrous ($S = 2$) and its *IS* changes to a value of 0.7 mm/s with *QS* ranging from 3.25 to 3.55 mm/s. These values set a reference to all other iron-sulfur centers.

Binuclear iron-sulfur centers, [2Fe–2S], can undergo one-electron reduction. The fully oxidized center is in the 2+ state since it has two high-spin ferric ions. For iron-sulfur centers with more than one iron, total oxidation state is determined based on the formal charge of iron and sulfur atoms, so in this case we have $2 \times (3+) + 2 \times (2-) = 2+$. The two ferric ions are antiferromagnetically coupled to yield a diamagnetic ground state ($S_{total} = 0$). The Mössbauer spectrum shows two almost equal quadrupole doublets with *IS* and *QS* approximately equal to 0.27 mm/s and 0.60 mm/s, respectively. The one-electron reduction (1+ state) gives rise to a paramagnetic $S_{total} = ½$ spin system. In the Mössbauer spectrum two components of equal intensity are now observable. One of these components can be attributed to sulfur coordinated high-spin ferric ion (*IS* and *QS* of 0.35 mm/s and 0.65 mm/s) while the other dramatically changes with *IS* and *QS* approximately equal to 0.60 mm/s and 2.70 mm/s, respectively. These values are closer to the ones obtained for the reduced rubredoxin-type site and support the existence of valence-trapped sites in this type of binuclear center. The $S_{total} = ½$ ground state can thus be explained by antiferromagnetically coupled high-spin ferric and ferrous ions. In certain cases, an additional one-electron reduction is possible, producing the fully reduced center with two high-spin ferrous ions antiferromagnetically coupled, resulting in a diamagnetic ground state with *IS* ranging from 0.70 to 0.81 mm/s and a *QS* ranging from 2.32 to 2.76 mm/s. One example of how Mossbauer can distinguish between different coordination types for otherwise similar centers is the so-called Rieske cluster. This type of center is almost identical to the [2Fe–2S], but in one of the irons the cys-

teinyl coordination is replaced by two histidine residues. In this case two resolved quadrupole doublets are observed, displaying higher *QS* and *IS* values.

One other well-known iron-sulfur center in nature is the [4Fe–4S]. This center is best described as a cubane-type structure with four iron ions at alternate vertices bound to four labile sulfur atoms and protein bound to four cysteinyl groups. Each iron retains an all sulfur coordination in an almost tetrahedral geometry. Four oxidation states are known for this center (3+ to 0) but each cluster will almost only cycle between two oxidation states. Centers cycling between the 2+/1+ oxidation states are the most common [4Fe–4S] centers and are both used in intra- and intermolecular electron transfer chains as well as enzyme active sites. In the 2+ state, with a diamagnetic ground state, the four iron ions are almost indistinguishable with *IS* around 0.45 mm/s and a *QS* ranging from 1.0 to 1.3 mm/s. These spectra can be explained by the presence of two valence-delocalized iron ion pairs ($S = 9/2$). The formal oxidation state of the iron ions in the pair is 2.5+. The two valence-delocalized pairs are antiferromagnetically coupled to produce the diamagnetic ground state. The one electron reduction produces a full ferrous pair ($S = 4$) with *IS* of approximately 0.60 mm/s, which remains antiferromagnetically coupled to the remaining valence-delocalized pair resulting in a $S_{total} = ½$ paramagnetic state. The oxidation state 0 ($S_{total} = 4$) is only known in a few examples, with all iron ions in the ferrous state displaying parameters typical of high-spin ferrous ions with sulfur coordination. Centers cycling between the 3+/2+ oxidation states are known as HIPIP centers (for High Potential Iron-sulfur Proteins). The 3+ state is explained by the presence of a full ferric pair with parameters typical of sulfur-coordinated high-spin ferric ions antiferromagnetically coupled to the remaining valence-delocalized pair resulting in a $S_{total} = ½$ paramagnetic state.

The [3Fe–4S] shares a similar cubane structure, but one of the vertices is now empty. It cycles between a 1+ state ($S_{total} = ½$) with all high-spin ferric ions having *IS* and *QS* of around 0.28 and 0.53 mm/s, respectively. The one electron reduction produces a valence-delocalized pair (S =9/2), with the extra iron ion remaining in the high-spin ferric state ($S = 5/2$) resulting in a system with a $S_{total} = 2$ ground state.

Iron-sulfur centers of higher nuclearity and mixed coordination state also exist. These more complex systems such as the P-cluster, MoFe-cofactor or novel tetranuclear hybrid cluster (Ravi et al. 1994; Bjornsson et al. 2017; Tavares et al. 1998) share some of the characteristics described above for the simpler systems.

Mössbauer spectroscopy can also help in identifying binding sites in the iron-sulfur cluster. This is of particular importance for enzyme active sites. The first substrate-bound observation was made for the enzyme aconitase, that contains a [4Fe–4S] center at the active site (Emptage et al. 1983). In this case the authors were able to determine a specific iron site that was able to bind citrate. Substrate binding resulted in a change to *IS* of 0.84–0.89 mm/s an *QS* of 1.26–1.83 mm/s, which are distinct from the previous typical [4Fe–4S] center parameters.

8.7.2 Heme Proteins

Heme proteins and enzymes are among the best studied systems in biology and among some of the first used in biological Mössbauer studies (Münck and Champion 1975). These proteins contain at least one heme prostetic group that can be covalently attached to the protein polypeptide chain and are involved in electron transfer processes, molecular oxygen storage and transport, detoxification, etc. Different heme groups can be found in nature, although the most common are heme *b*, *a* and *c*. The heme basic structure is an iron ion tetracoordinated by a porphyrin. Heme cofactors differ on the tetrapyrrole rings substituents and the number and type of axial coordination, that can be an amino acid side chain (e.g. histidine, cysteine, methionine or tyrosine residues), or small molecules (e.g. molecular oxygen, nitric oxide, nitrite, water, hydroxide). Mössbauer spectroscopy has played an important role in the characterization of heme structure and catalytic activity, either helping to identify the nature of axial ligands or by enabling the study of oxidation states difficult to probe by other techniques, such as the ferrous and ferryl heme states.

In the high-spin ferric state heme proteins display quite complex spectra and several measurements at variable temperature and field need to be performed to properly characterize such a system. Fortunately, in this redox state heme cofactors are EPR active and correlation with EPR results greatly simplifies Mössbauer data analysis. Typically, *IS* and *QS* ranging from 0.35 to 0.45 mm/s and 0.5 to 1.5 mm/s, respectively, are observed. Heme cofactors can also be found in the low-spin ferric heme state. Sometimes this state is promoted by the binding of divalent ions or by temperature changes. In this case it is helpful to use the method propose by Griffith for the binding of azide to hemoglobin (Griffith 1957). This state has distinctive *IS* and *QS*, ranging from 0.15 to 0.25 mm/s and 1.5 to 2.5 mm/s.

Heme cofactors can undergo one-electron reduction in which case they become either high-spin ferrous ($S = 2$) or low-spin ferrous ($S = 0$). Both states can be properly analyzed by Mössbauer spectroscopy with particular emphasis on the high-spin ferrous state, for which a detailed description of the electronic structure is possible. Characteristic values of *IS* and *QS* are observed, with high-spin ferrous heme cofactors having *IS* and *QS* ranging from 0.85 to 1.0 mm/s and 1.5 to 3.0 mm/s, while for the low-spin case *IS* varies between 0.30 and 0.45 mm/s with *QS* being less than 1.5 mm/s.

Under catalytic conditions it is possible to obtain a more oxidized ferryl (Fe^{4+}) state. The characterized reaction intermediates show a small *IS* value, between 0.0 and 0.1 mm/s, and *QS* of 1.0–2.0 mm/s.

8.7.3 Non-heme Iron Centers

Enzymes containing non-heme iron perform important biological reactions, in most cases involving molecular oxygen or reactive oxygen species. For all purposes the

iron cofactors that are not iron-sulfur centers or heme cofactors are considered to be non-heme iron centers and are usually referred to as iron cofactors with nitrogen and/or oxygen containing ligands. However, in some known cases, a cysteine residue will contribute to the coordination sphere. Essentially, two types of centers exist. Monomeric centers such as the ones present in dioxygenases and superoxide reductases (Zimmermann et al. 1978; Tavares et al. 1994; Pereira et al. 2007) or μ-oxo, μ-hydroxo or peroxo diiron centers like the ones found in ribonucleotide reductase, methane monooxygenase or ferritin (Bollinger et al. 1991; Fox et al. 1993; Pereira et al. 1997).

Monomeric iron sites will have three attainable redox states. In the ferric state the center is a high-spin system ($S = 5/2$) with *IS* of 0.40–0.6 mm/s and $QS =$ 0.5–1.5 mm/s. Mössbauer is sensitive to small changes in the coordination sphere and it is expected that the lower *IS* values in that range be from 5-coordinated and/or from additional single cysteine residue coordination. In one known case, the enzyme nitrile hydratase, the monomeric ferric center is present in the low-spin state ($S =$ 1/2). This is mainly due to the fact that the coordination sphere is constituted by three cysteinyl residues (two of them are post-translationally modified to cysteine sulfinic and cysteine sulfenic acid forms) and two deprotonated backbone amides from a serine and a cysteine residue (Mascharak 2013). This quite unique coordination sphere will result in a smaller than expected $IS = 0.25$ mm/s consistent with a low-spin ferric configuration (Popescu et al. 2001). Monomeric centers can be reduced to the ferrous state. In the high-spin ferrous configuration the site parameters are very similar to other high-spin ferrous complexes, with $IS =$ 1.1–1.3 mm/s and $QS =$ 2.0–3.2 mm/s. Under catalytic conditions that require molecular oxygen activation, a high-spin oxoferryl ($S = 2$) state was detected for the enzyme taurine/α-ketoglutarate dioxygenase (Price et al. 2003). In this case the authors report an $IS = 0.31$ mm/ and $QS = 0.88$ mm/s. Also, in a superoxide reductase enzyme system, upon reaction with hydrogen peroxide, another intermediate species with *IS* of 0.54 mm/s and *QS* of 0.80 mm/s was found (Horner et al. 2004). This was proposed to be a high-spin side-on ferric peroxo species.

Dinuclear non-heme iron centers are quite important in nature and have been reported in several cases either as a cofactor or as an intermediate species of iron-processing reactions. This type of centers consists of two iron atoms each with nitrogen and/or oxygen containing ligands (usually carboxylate and imidazole groups) and at least one bridging carboxylate group. The type and number of non-bridging ligands, as well as the availability of an open coordination site will determine if molecular oxygen will bind reversible. Depending on the reactivity of the center, an additional bridging carboxylate, oxo/hydroxo or peroxo group can be found. Such structural plasticity makes this type of centers well suited for a number of different functions from simple oxygen transport (hemerythrin) (Clark and Webb 1981; Stenkamp 1994), to having key roles in DNA biosynthesis (ribonucleotide reductase) (Atkin et al. 1973; Stubbe et al. 2003), hydrocarbon oxidation (methane monooxygenase, toluene/*o*-xylene monooxygenase or phenol hydroxylase) (Fox et al. 1993; Sazinsky and Lippard 2006; Cadieux et al. 2002; Murray et al. 2006), iron biomineralization (ferritins) (Liu and Theil 2005; Pereira et al. 1997, 2012), regulation of cell

proliferation (deoxyhypusine hydroxylase) (Vu et al. 2009) or fatty acid desaturation (Δ^9 stearoyl-acyl carrier protein desaturase) (Shanklin et al. 1997, 2009).

Dinuclear non-heme iron centers are known to have five oxidation states where iron ions formal oxidation state range from 2+ to 4+. The all ferrous state Mössbauer spectra shows two very similar quadrupole doublets with high-spin ferrous characteristic parameters (*QS* varying from 2.7 to 3.1 mm/s and *IS* of approximately 1.3 mm/s). When both iron ions are in the ferrous state the center binds molecular oxygen and, in most cases, intermediate species of higher oxidation states are generated. The type and number of reaction intermediates depends on the type of catalysis, but an almost ubiquitous first intermediate is a peroxodiiron species. In this case two ferric irons are antiferromagnetically couple producing a diamagnetic ground state ($S_{total} = 0$). In all but one cases, the peroxodiiron intermediate shows a visible band with λ_{max} between 620 and 720 nm (ε of 1000–1500 M^{-1} cm^{-1}) as well as *IS* between 0.55 and 0.68 mm/s and *QS* higher than 0.9 mm/s. The known exception is an intermediate found in the Toluene/*o*-Xylene Monooxygenase Hydroxylase component which has distinctive *IS* and *QS* Mössbauer parameters (0.67 and 0.54 mm/s, respectively), also lacking an observable UV-visible absorption band. Quite interestingly, a crystal structure of a peroxodiferric intermediate was possible to obtain in a Deoxyhypusine Hydroxylase, only possible due to the extreme unusual longevity of such peroxo intermediate (Han et al. 2015).

Under catalytic conditions, and after O–O bond cleavage, two other states of dinuclear non-heme iron centers were observed. These are high-valent iron species formed in soluble methane monooxygenase hydroxylase component (MMOH) and ribonucleotide reductase subunit R2 (RNR-R2) proteins. In the case of MMOH an all ferryl intermediate was detected. The so-called intermediate Q has *IS* of 0.14–0.21 mm/s and *QS* of 0.53–0.68 mm/s and exhibits a bis-μ-oxo diamond core structure (Lee et al. 1993; Liu et al. 1994; Banerjee et al. 2015). The low *IS* value is indicative of a formal oxidation state of 4+. Akin of what was reported to the peroxodiferric intermediate, high-field spectra show this intermediate to be diamagnetic. For the case of RNR-R2, Mössbauer spectroscopy was successfully used to characterize another high-valent iron species. In this case the so-called intermediate X was characterized as being "a spin-coupled Fe^{3+}/Fe^{4+} center without a radical, but with significant spin delocalization onto the oxygen ligands". In this case the two iron sites show *IS* of 0.56 and 0.26 mm/s, which can be assigned to a high-spin ferric ($S = 5/2$) and a high-spin ferryl ($S = 4$), antiferromagnetically coupled to produce a paramagnetic ground state ($S_{total} = ½$) (Sturgeon et al. 1996).

Interestingly, it was possible to use Mössbauer spectroscopy to probe the similarity between Q and X intermediates. Since Q is formally in a one-electron more oxidized state than X, reduction of Q could produce X if intermediate structures are similar. The Mössbauer spectra of a sample obtained by cryoreduction of intermediate Q clearly show the appearance of a mixed-valent Fe^{3+}/Fe^{4+} center with parameters similar to intermediate X, which reinforces the assignment done in the intermediate Q spectroscopic analysis (Valentine et al. 1998).

The above cited kinetic intermediates will eventually decay into an all ferric dinuclear iron center, which shows a diamagnetic ground state ($S_{total} = 0$) and can be

explained by two similar quadrupole doublets with Mössbauer parameters typical of high-spin ferric ions (*QS* varying from 1.0 to 1.9 mm/s and *IS* of 0.45 to 0.55 mm/s).

Dinuclear non-heme iron centers can also occur in a mixed-valence oxidation state, also known as semimet form reminiscent of a nomenclature first used for hemerythrin proteins. Generated by one electron reduction of the differic form, a system with spin-coupled Fe^{3+}/Fe^{2+} center is obtained. The Mössbauer spectrum shows two quadrupole doublets with parameters typical of high-spin ferric and ferrous ions supporting a localized mixed-valence state.

8.7.4 Iron Cores

Iron is an essential element that, as seen so far, mainly contributes as a cofactor of many different proteins and enzymes. The bioavailability of iron at physiological conditions is poor, due to its low solubility in aqueous solutions. The ferric form is extremely insoluble, whereas the ferrous form is relatively soluble, although very toxic in the presence of molecular oxygen, potentiating the non-enzymatic production of reactive oxygen species (ROS) that cause oxidative damage of cellular components, contributing to the development of cancer, neurodegenerative and cardiac diseases, and many other pathophysiological conditions. As such, organisms have developed mechanisms to acquire and concentrate iron and thus resist to ROS toxic effects, keeping an effective iron homeostasis. In all organisms, iron is stored by proteins from the ferritin-family: In eukaryotes by canonical ferritins, (Ft) and in prokaryotes by bacterial ferritins (Ftn), heme-containing bacterioferritins (Bfr) or by Dps (DNA-binding protein from starved cells). With exception of Dps that are 12-oligomers, all other ferritins are composed of 24 subunits (24-mer) organized into a hollow spherical protein shell. Most ferritin molecules from higher eukaryotic organisms are heteropolymers, containing two types of subunits that differ on their molecular masses, the L (ca. 19 kDa) and H subunit (ca. 21 kDa). The H subunits catalyze the initial step of rapid oxidation of ferrous ions (ferroxidation) due to the presence of a catalytic center (ferroxidase center) and direct the oxidized ferric species into the inner cavity, while the L subunits promote the formation of the mineral core (mineralization). Prokaryotic ferritins are homopolymers composed of subunits more homologous to H. The protein inner cavity size, of approximately 8 nm, that can store up to 4,500 iron atoms in the form of a ferrihydrite mineral. Dps inner cavities are smaller (ca. 5 nm) forming iron mineral cores of as much as 500 iron. However, for both cases, iron particles can be smaller with as little as 48 iron ions showing core related properties (Yang et al. 1987; Pereira et al. 1997; Penas et al. 2018). At low temperature, the characteristic Mössbauer spectra of iron cores is composed of a magnetic sextet. Raising the acquisition temperature leads to a conversion of the magnetic sextet into central quadrupole doublets. The temperature at which the doublet and sextet components have equal intensity is defined as the blocking temperature, T_B (Mørup and Topsøe 1976; Coey et al. 1984; St Pierre et al. 1986). T_B is linearly proportional to particle volume (V) and to the magnetic anisotropy

constant (K) which are a function of material characteristics such as particle size and mass density. Because iron cores are ferrihydrite particles with poor crystallinity, a distribution of hyperfine parameters is needed to fully explain the magnetic spectrum (Rancourt and Ping 1991). At higher temperatures the spectrum can be explained by two or more quadrupole doublets with *IS* ranging from 0.47 to 0.54 and *QS* of 0.57 to 1.2 mm/s. It was also shown that iron cores can oxidize and incorporate additional ferrous ions (Penas et al. 2018). In this case the incorporation is accompanied by the appearance of a new iron species with *IS* of 0.7 mm/s and *QS* of 2.10 mm/s, which was explained as mixed-valence iron species due to fast electron hopping between iron pairs in the core mineral.

8.7.5 Whole Cell Mössbauer Spectroscopy

Mössbauer spectroscopy has been also successfully applied to whole cells, contributing to explain differences in distribution of cellular iron content. Some of these studies benefit from either ^{57}Fe enrichment or the use of overexpression systems. Careful analysis makes possible to sort different groups of Fe-containing species such as high-spin ferric ions (ferritin, non-heme centers with N and O ligands), low-spin heme ferric ions, iron-sulfur centers and high-spin ferrous ions. The use of Mössbauer spectroscopy enabled the study of in vivo behavior of (overexpressed) FNR protein (regulator of fumarate and nitrate reduction) and pyruvate formate-lyase activating enzyme showing the molecular oxygen dependent iron-sulfur center interconversion (Popescu et al. 1998; Yang et al. 2009). Whole cell Mössbauer spectroscopy was also used to demonstrate that iron sulfur centers present in purified recombinant biotin synthase were present in vivo, not being an artifact of the protein purification procedure, establishing that under aerobic growth this protein is expressed in an inactive form (Cosper et al. 2002). Studies were also done in *Escherichia coli* cells (wild-type and cell variants with deletion of ferric uptake regulatory protein—Fur, and different ferritins—Ftn, Bfr, and Dps) grown with different iron concentrations, carbon sources, aerobic or anaerobic conditions, and harvested in different growth phases (Wofford 2019). These studies point to a respiratory shield that protects a low-molecular-mass ferrous iron pool from molecular oxygen dependent oxidation, showing that the iron content of *Escherichia coli* cells is very similar to what was found for mitochondria. Mössbauer spectroscopy has also been applied to unambiguously detect and quantify all hemoglobin forms present in blood samples (Khvastunov et al. 2013).

Acknowledgements The Portuguese National Funding Agency FCT-MCTES through Research Grants POCTI/QUI/37413/2001, POCTI/QUI/47273/2002, POCI/QUI/57475/2004, PTDC/QUI/64248/2006, PTDC/QUI/67142/2006, PTDC/SAU-SAP/111482/2009, PTDC/BIA-PRO/111485/2009, and PTDC/OCE-ETA/32567/2017. This work was also supported by Radiation Biology and Biophysics Doctoral Training Programme (RaBBiT, PD/00193/2010); UID/Multi/04378/2019 (UCIBIO); UID/FIS/00068/2013 (CEFITEC). UID/Multi/04349/2013 (C2TN).

References

Atkin CL, Thelander L, Reichard P, Lang G (1973) Iron and free radical in ribonucleotide reductase. Exchange of iron and Mössbauer spectroscopy of the protein B2 subunit of the *Escherichia coli* enzyme. J Biol Chem 248(21):7464–7472

Baggio-Saitovitch E, Berry FJ, De Waard H, Greneche JM, Gütlich P, Stevens J (2002) New recommendations for nomenclature and the reporting of Mössbauer data. IBAME (International Board on the Applications of the Mössbauer Effect). https://app.box.com/s/9pun6671zzdhyh16myb6f7dypz4mtgud

Banerjee R, Proshlyakov Y, Lipscomb JD, Proshlyakov DA (2015) Structure of the key species in the enzymatic oxidation of methane to methanol. Nature 518(7539):431–434. https://doi.org/10.1038/nature14160

Bjornsson R, Neese F, DeBeer S (2017) Revisiting the Mössbauer isomer shifts of the FeMoco cluster of nitrogenase and the cofactor charge. Inorg Chem 56(3):1470–1477. https://doi.org/10.1021/acs.inorgchem.6b02540

Bollinger JM Jr, Edmondson DE, Huynh BH, Filley J, Stubbe J (1991) Mechanism of assembly of the tyrosyl radical-dinuclear iron cluster cofactor of ribonucleotide reductase. Science 253(5017):292–298. https://doi.org/10.1126/science.1650033

Cadieux E, Vrajmasu V, Achim C, Powlowski J, Münck E (2002) Biochemical, Mössbauer, and EPR studies of the diiron cluster of phenol hydroxylase from pseudomonassp. Strain CF 600. Biochemistry 41(34):10680–10691. http://doi.org/10.1021/bi025901u

Clark PE, Webb J (1981) Mössbauer spectroscopic studies of hemerythrin from *Phascolosoma lurco* (syn. *Phascolosoma arcuatum*). Biochemistry 20(16):4628–4632. http://doi.org/10.1021/bi00519a017

Coey JMD, Meagher A, Kelly JM, Vos JG (1984) A Mössbauer study of polymers prepared from polyvinylpyridine and ferric chloride or ferric nitrate. J Polym Sci Part A: Polym Chem 22(2):303–318. http://doi.org/10.1002/pol.1984.170220203

Cosper MM, Jameson GNL, Eidsness MK, Huynh BH, Johnson MK (2002) Recombinant *Escherichia coli* biotin synthase is a [2Fe-2S](2+) protein in whole cells. FEBS Lett 529(2–3):332–336. https://doi.org/10.1016/S0014-5793(02)03390-2

Emptage MH, Kent TA, Kennedy MC, Beinert H, Münck E (1983) Mössbauer and EPR studies of activated aconitase: development of a localized valence state at a subsite of the [4Fe-4S] cluster on binding of citrate. Proc Natl Acad Sci USA 80(15):4674–4678. https://doi.org/10.1073/pnas.80.15.4674

Fox BG, Hendrich MP, Surerus KK, Andersson KK, Froland WA, Lipscomb JD, Münck E (1993) Moessbauer, EPR, and ENDOR studies of the hydroxylase and reductase components of methane monooxygenase from *Methylosinus trichosporium* OB3b. J Am Chem Soc 115(9):3688–3701. http://doi.org/10.1021/ja00062a039

Frauenfelder H (1962) The Mössbauer effect. W. A. Benjamin Inc., New York

Greenwood NN, Gibb TC (1971) Mössbauer spectroscopy. Chapman and Hall, Ltd., London

Griffith JS (1957) Binding in hæmoglobin azide as determined by electron resonance: theory of electron resonance in ferrihæmoglobin azide. Nature 180(4575):30–31. https://doi.org/10.1038/180030a0

Gütlich P, Bill E, Trautwein AX (2011) Mössbauer spectroscopy and transition metal chemistry, 1st edn. Springer, Berlin, Heidelberg

Han Z, Sakai N, Böttger LH, Klinke S, Hauber J, Trautwein AX, Hilgenfeld R (2015) Crystal structure of the peroxo-diiron(III) intermediate of deoxyhypusine hydroxylase, an oxygenase involved in hypusination. Structure 23(5):882–892. https://doi.org/10.1016/j.str.2015.03.002

Horner O, Mouesca J-M, Oddou J-L, Jeandey C, Nivière V, Mattioli TA et al (2004) Mössbauer characterization of an unusual high-spin side-on peroxo−Fe^{3+} species in the active site of superoxide reductase from *Desulfoarculus baarsii*. Density functional calculations on related models. Biochemistry 43(27):8815–8825. http://doi.org/10.1021/bi0498151

Khvastunov SM, Novakova AA, Kiseleva TY (2013) Applying Mössbauer spectroscopy to studies of red blood cells in donated blood. Bull Russ Acad Sci: Phys 77(6):726–729. http://doi.org/10.3103/S1062873813060178

Lang G, Marshall W (1966) Mössbauer effect in some haemoglobin compounds. Proc Phys Soc Lond 87:3–34. https://doi.org/10.1016/S0022-2836(66)80032-3

Lee SK, Fox BG, Froland WA, Lipscomb JD, Münck E (1993) A transient intermediate of the methane monooxygenase catalytic cycle containing an $Fe^{IV}Fe^{IV}$ cluster. J Am Chem Soc 115(14):6450–6451. https://doi.org/10.1021/ja00067a086

Liu X, Theil EC (2005) Ferritins: dynamic management of biological iron and oxygen chemistry. Acc Chem Res 38(3):167–175. https://doi.org/10.1021/ar0302336

Liu KE, Wang D, Huynh BH, Edmondson DE, Salifoglou A, Lippard SJ (1994) Spectroscopic detection of intermediates in the reaction of dioxygen with the reduced methane monooxygenase/hydroxylase from *Methylococcus capsulatus* (bath). J Am Chem Soc 116(16):7465–7466. https://doi.org/10.1021/ja00095a083

Long GJ, Cranshaw TE, Longworth G (1983) The ideal Mössbauer effect absorber thicknesses. Mossb Effect Ref Data J 6(2):42–49. https://doi.org/10.1016/0029-554X(80)90872-1

Mascharak PK (2013) The active site of nitrile hydratase: an assembly of unusual coordination features by nature. In: Molecular design in inorganic biochemistry, vol 160. Springer Berlin Heidelberg, Berlin, Heidelberg, pp 89–113. http://doi.org/10.1007/430_2012_85

Mørup S, Topsøe H (1976) Mössbauer studies of thermal excitations in magnetically ordered microcrystals. Appl Phys 11(1):63–66. https://doi.org/10.1007/BF00895017

Münck E, Champion PM (1975) Heme proteins and model compounds: Mössbauer absorption and emission spectroscopy. Ann N Y Acad Sci 244(1):142–162. https://doi.org/10.1111/j.1749-6632.1975.tb41528.x

Murray LJ, García-Serres R, Naik S, Huynh BH, Lippard SJ (2006) Dioxygen activation at non-heme diiron centers: characterization of intermediates in a mutant form of toluene/o-xylene monooxygenase hydroxylase. J Am Chem Soc 128(23):7458–7459. https://doi.org/10.1021/ja062762l

Pandelia M-E, Lanz ND, Booker SJ, Krebs C (2015) Mössbauer spectroscopy of Fe/S proteins. Biochim Biophys Acta Mol Cell Res 1853(6):1395–1405. http://doi.org/10.1016/j.bbamcr.2014.12.005

Penas D, Pereira AS, Tavares P (2018) Direct evidence for ferrous ion oxidation and incorporation in the absence of oxidants by Dps from *Marinobacter hydrocarbonoclasticus*. Angew Chem Int Ed 58(4):1013–1018. http://doi.org/10.1002/anie.201809584

Pereira AS, Tavares P, Lloyd SG, Danger D, Edmondson DE, Theil EC, Huynh BH (1997) Rapid and parallel formation of Fe^{3+} multimers, including a trimer, during H-type subunit ferritin mineralization. Biochemistry 36(25):7917–7927. https://doi.org/10.1021/bi970348f

Pereira AS, Tavares P, Folgosa F, Almeida RM, Moura I, Moura JJG (2007) Superoxide reductases. Eur J Inorg Chem 2007(18):2569–2581. https://doi.org/10.1002/ejic.200700008

Pereira AS, Timoteo CG, Guilherme M, Folgosa F, Naik SG, Duarte AG et al (2012) Spectroscopic evidence for and characterization of a trinuclear ferroxidase center in bacterial ferritin from *Desulfovibrio vulgaris* Hildenborough. J Am Chem Soc 134(26):10822–10832. https://doi.org/10.1021/ja211368u

Popescu CV, Bates DM, Beinert H, Münck E, Kiley PJ (1998) Mössbauer spectroscopy as a tool for the study of activation/inactivation of the transcription regulator FNR in whole cells of *Escherichia coli*. Proc Natl Acad Sci USA 95(23):13431–13435. https://doi.org/10.1073/pnas.95.23.13431

Popescu V-C, Münck E, Fox BG, Sanakis Y, Cummings JG, Turner IM, Nelson MJ (2001) Mössbauer and EPR studies of the photoactivation of nitrile hydratase. Biochemistry 40(27):7984–7991. https://doi.org/10.1021/bi010198f

Price JC, Barr EW, Tirupati B, Bollinger JM, Krebs C (2003) The first direct characterization of a high-valent iron intermediate in the reaction of an α-ketoglutarate-dependent dioxygenase: a high-spin Fe(IV) complex in taurine/α-ketoglutarate dioxygenase (TauD) from *Escherichia coli*. Biochemistry 42(24):7497–7508. https://doi.org/10.1021/bi030011f

Rancourt DG, Ping JY (1991) Voigt-based methods for arbitrary-shape static hyperfine parameter distributions in Mössbauer spectroscopy. Nucl Instrum Methods Phys Res B 58(1):85–97. http://doi.org/10.1016/0168-583X(91)95681-3

Rancourt DG, McDonald AM, Lalonde AE, Ping JY (1993) Mössbauer absorber thicknesses for accurate site populations in Fe-bearing minerals. Amer Miner 78:17

Ravi N, Moore V, Lloyd SG, Hales BJ, Huynh BH (1994) Mössbauer characterization of the metal clusters in *Azotobacter vinelandii* nitrogenase VFe protein. J Biol Chem 269(33):20920–20924

Sazinsky MH, Lippard SJ (2006) Correlating structure with function in bacterial multicomponent monooxygenases and related diiron proteins. Acc Chem Res 39(8):558–566. https://doi.org/10.1021/ar030204v

Shanklin J, Achim C, Schmidt H, Fox BG, Münck E (1997) Mössbauer studies of alkane omega-hydroxylase: evidence for a diiron cluster in an integral-membrane enzyme. Proc Natl Acad Sci USA 94(7):2981–2986. https://doi.org/10.1073/pnas.94.7.2981

Shanklin J, Guy JE, Mishra G, Lindqvist Y (2009) Desaturases: emerging models for understanding functional diversification of diiron-containing enzymes. J Biol Chem 284(28):18559–18563. https://doi.org/10.1074/jbc.R900009200

St Pierre TG, Bell SH, Dickson DP, Mann S, Webb J, Moore GR, Williams RJ (1986) Mössbauer spectroscopic studies of the cores of human, limpet and bacterial ferritins. Biochim Biophys Acta 870(1):127–134. https://doi.org/10.1016/0167-4838(86)90015-4

Stenkamp RE (1994) Dioxygen and hemerythrin. Chem Rev 94(3):715–726. https://doi.org/10.1021/cr00027a008

Stubbe J, Nocera DG, Yee CS, Chang MCY (2003) Radical initiation in the class I ribonucleotide reductase: long-range proton-coupled electron transfer? Chem Rev 103(6):2167–2202. https://doi.org/10.1021/cr020421u

Sturgeon BE, Burdi D, Chen S, Huynh BH, Edmondson DE, Stubbe J, Hoffman BM (1996) Reconsideration of X, the diiron intermediate formed during cofactor assembly in *E. coli* ribonucleotide reductase. J Am Chem Soc 118(32):7551–7557. http://doi.org/10.1021/ja960399k

Tavares P, Ravi N, Moura JJ, LeGall J, Huang YH, Crouse BR et al (1994) Spectroscopic properties of desulfoferrodoxin from *Desulfovibrio desulfuricans* (ATCC 27774). J Biol Chem 269(14):10504–10510

Tavares P, Pereira AS, Krebs C, Ravi N, Moura JJ, Moura I, Huynh BH (1998) Spectroscopic characterization of a novel tetranuclear Fe cluster in an iron-sulfur protein isolated from *Desulfovibrio desulfuricans*. Biochemistry 37(9):2830–2842. https://doi.org/10.1021/bi9723008

Valentine AM, Tavares P, Pereira AS, Davydov R, Krebs C, Hoffman BM et al (1998) Generation of a mixed-valent $Fe^{(III)}Fe^{(IV)}$ form of intermediate Q in the reaction cycle of soluble methane monooxygenase, an analog of intermediate X in ribonucleotide reductase R2 assembly. J Am Chem Soc 120(9):2190–2191. https://doi.org/10.1021/ja974169x

Vu VV, Emerson JP, Martinho M, Kim YS, Münck E, Park MH, Que L (2009) Human deoxyhypusine hydroxylase, an enzyme involved in regulating cell growth, activates O_2 with a non-heme diiron center. Proc Natl Acad Sci USA 106(35):14814–14819. https://doi.org/10.1073/pnas.0904553106

Wertheim GK (1964) Mössbauer effect: principles and applications. Academic Press Inc., London

Wofford JD, Bolaji N, Dziuba N, Outten FW, Lindahl PA (2019) Evidence that a respiratory shield in Escherichia coli protects a low-molecular-mass FeII pool from O2-dependent oxidation. J Biol Chem 294(1):50–62. http://doi.org/10.1074/jbc.RA118.005233

Yang CY, Meagher A, Huynh BH, Sayers DE, Theil EC (1987) Iron(III) clusters bound to horse spleen apoferritin: an X-ray absorption and Mössbauer spectroscopy study that shows that iron nuclei can form on the protein. Biochemistry 26(2):497–503. https://doi.org/10.1021/bi00376a023

Yang J, Naik SG, Ortillo DO, García-Serres R, Li M, Broderick WE et al (2009) The iron–sulfur cluster of pyruvate formate-lyase activating enzyme in whole cells: cluster interconversion and a valence-localized $[4Fe\text{-}4S]^{2+}$ state. Biochemistry 48(39):9234–9241. https://doi.org/10.1021/bi9010286

Zimmermann R, Huynh BH, Münck E, Lipscomb JD (1978) High-field Mössbauer studies of reduced protocatechuate 3,4-dioxygenase. J Chem Phys 69(12):5463–5467. https://doi.org/10.1063/1.436538